APPLIED SCIENCES AND ENGINEERING

Metasurface spectrometers beyond resolution-sensitivity constraints

Feng Tang[1,2]†, Jingjun Wu[1,3]†, Tom Albrow-Owen[4]†, Hanxiao Cui[5]†, Fujia Chen[2,6], Yaqi Shi[2,6], Lan Zou[7], Jun Chen[1], Xuhan Guo[8], Yijun Sun[2,6], Jikui Luo[2,6], Bingfeng Ju[6], Jing Huang[7], Shuangli Liu[7], Bo Li[1], Liming Yang[3], Eric A. Munro[4], Wanguo Zheng[3], Hannah J. Joyce[4], Hongsheng Chen[2,6], Lufeng Che[2], Shurong Dong[2,6], Zhipei Sun[9], Tawfique Hasan[4]*, Xin Ye[1,7]*, Yihao Yang[2,6]*, Zongyin Yang[2,6]*

Conventional spectrometer designs necessitate a compromise between their resolution and sensitivity, especially as device and detector dimensions are scaled down. Here, we report on a miniaturizable spectrometer platform where light throughput onto the detector is instead enhanced as the resolution is increased. This planar, CMOS-compatible platform is based around metasurface encoders designed to exhibit photonic bound states in the continuum, where operational range can be altered or extended simply through adjusting geometric parameters. This system can enhance photon collection efficiency by up to two orders of magnitude versus conventional designs; we demonstrate this sensitivity advantage through ultralow-intensity fluorescent and astrophotonic spectroscopy. This work represents a step forward for the practical utility of spectrometers, affording a route to integrated, chip-based devices that maintain high resolution and SNR without requiring prohibitively long integration times.

INTRODUCTION

Optical spectroscopy plays an essential role across scientific research and industry for noncontact materials analysis (*1*–*3*), increasingly through in situ or portable platforms (*4*–*6*). A central aim in optical device design is to make the most efficient use of photons available and, in doing so, extract as much information as possible from incident radiation. This is especially the case when looking to accurately characterize low-intensity light spectra and of particular importance for miniaturized systems working in situ with uncontrolled or ambient illumination; here, the efficiency or sensitivity of a system dictates its capability to collect data with satisfactory resolution in a given timeframe (*7*). However, a major constraint in (miniaturized) spectrometer design lies in an inherent trade-off between the resolution and sensitivity of devices. For platforms based on conventional strategies (e.g., those using grating-mediated dispersion or filter arrays), higher resolutions have typically had to come at the expense of the transmitted light intensity incident onto the detectors, leading to decreasing signal-to-noise ratios (SNRs) and longer integration times (*8*, *9*). This limitation can be described via the resolution-luminosity product (*8*), $E = RL$, (where R is the resolution and L is the luminosity, the light throughput from the source onto the detectors), given that the device's efficiency, E, is constant for a given sensing area. Now, the most feasible option for moving beyond this constraint is to use cooled, high-sensitive detectors (*10*), an impractical solution for many in situ or portable devices.

Here, we report on a microspectrometer platform based around dielectric metasurface encoders, which overcome these limitations by exploiting photonic quasi-bound states in the continuum (qBICs) (*11*). These encoders, combined with a computational reconstruction algorithm (*4*, *12*–*14*), enable a platform where detector flux in the device increases with resolution, affording a notably more efficient system, where high sensitivity and performance can be simultaneously realized. Through excitation intensity-resolved fluorescence spectroscopy of bacteria samples and telescopic planetary spectroscopy under different visibility conditions, we demonstrate the strengths of this system in being able to perform sensitive analyses under ultralow irradiance, all while in a highly miniaturized form factor. These microspectrometers could afford notable advances for lab-on-a-chip–, drone-, or satellite-based detection of subtle signals in applications such as trace chemical analysis, nanoscale biomedical sensing (*7*), or astrophotonics (*15*). Furthermore, the planar, complementary metal-oxide semiconductor (CMOS)–compatible nature of the platform, requiring only a single lithographic patterning step, would allow for straightforward manufacture of a device array onto a CMOS imaging sensor. This could offer a route toward highly sensitive snapshot spectral imaging cameras that do not require any complex optics or moving parts.

RESULTS

Bandstop strategy

The schematic in Fig. 1A illustrates the comparison of sensitivity between bandpass and bandstop strategies. A bandstop system can transmit the same portion of spectral information while losing fewer photons. Figure 1B shows the differences in operational principle between our qBIC bandstop array spectrometer and conventional bandpass grating or filter array systems. In the latter, each detector reads light with a single wavelength component that comes from

[1]Mianyang Sci-Tech City Institute of Photon Technology, Mianyang 621025, China. [2]College of Information Science and Electronic Engineering, Zhejiang University, Hangzhou 310027, China. [3]School of Electronic and Optical Engineering, Nanjing University of Science and Technology, Nanjing 210094, China. [4]Department of Engineering, University of Cambridge, Cambridge CB3 0FA, UK. [5]School of Aeronautics and Astronautics, Sichuan University, Chengdu 610065, China. [6]ZJU-Hangzhou Global Science and Technology Innovation Center and ZJU-UIUC Institute, Zhejiang University, Hangzhou 310027, China. [7]School of Information Engineering and School of Life Science and Engineering, Southwest University of Science and Technology, Mianyang 621010, China. [8]Department of Electronic Engineering, Shanghai Jiao Tong University, Shanghai 200240, China. [9]Department of Electronics and Nanoengineering, Aalto University, Espoo FI-00076, Finland.
*Corresponding author. Email: yangzongyin@zju.edu.cn (Z.Y.); xinye@swust.edu.cn (X.Y.); th270@cam.ac.uk (T.H.); yangyihao@zju.edu.cn (Y.Y.)
†These authors contributed equally to this work.

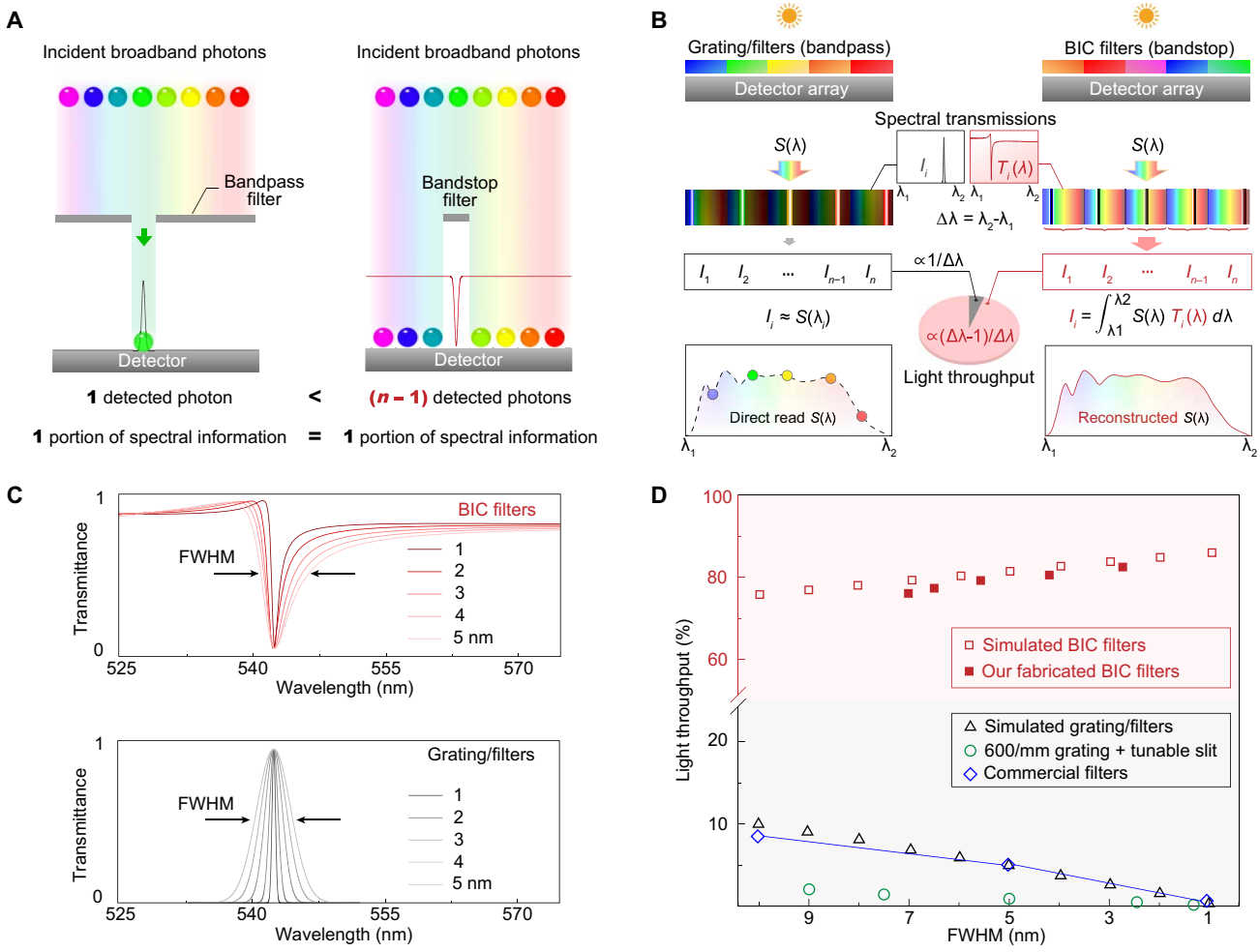

Fig. 1. Bandstop strategy for BIC-inspired spectrometer design. (**A** and **B**) Comparison of bandpass and bandstop strategies when designing a filter-array based spectrometer. (**C**) Simulated bandpass and qBIC bandstop features. (**D**) Light throughput as a function of the FWHM of transmission features under illumination of a broadband light (500 to 600 nm), as transmitted through simulated and commercial grating- and filter-based system with varying values of transmission FWHM.

gratings or narrow bandpass filters. The number of filters and their characteristic full width at half maximum (FWHM) dictate the effective resolution that such a system can achieve. Intuitively, given the nature of a bandpass transmission profile, where light outside of a target wavelength component is blocked, higher resolution (a narrower FWHM for each filter) necessarily results in lower flux and sensitivity.

A qBIC filter instead transmits the inverse, reflecting a narrow band of wavelengths. The characteristic transmission spectrum of a qBIC metasurface contains a collapsing Fano feature, resembling a "bandstop" profile (*16*, *17*). We integrate a range of different qBIC metasurfaces onto a CMOS detector array to create a computational spectrometer device, in which wavelength components are not directly read, but where the qBICs are used to encode spectral information into the electronic responses of the sensors beneath them. An algorithm is developed to then reconstruct the spectra of incident light by solving the inverse problem posed by these bandstop encoders. Crucially, we show that the light throughput in a qBIC-based system is not only at least an order of magnitude higher than that of a bandpass system for broadband light, but the intensity is also proportional to the resolution or FWHM of the spectral feature (see section S1), rather than inversely proportional as seen in Fig. 1, C and D. This qBIC-based scheme offers a route toward highly sensitive yet high-resolution microspectrometers.

Bound states in the continuum

We first present simulations and experimentally demonstrate the physics of the qBIC encoders, which underpin our platform. BICs are localized states with an infinitely long lifetime in the radiation continuum (*11*); they usually manifest in the form of quasi-bound states (*18*), which can couple to the surrounding environment with notably enhanced light-matter interaction. They have demonstrated potential in a range of applications, such as low-threshold micro-/nanolasers (*19*), high-sensitivity biosensors (*16*, *17*), and ultrafast vortex beam generators (*20*), although have yet to be applied toward spectroscopy. Figure 2A shows a schematic of the dielectric qBIC metasurface designed for this work, consisting of an array of cylindrical nanoholes arranged in a square lattice. Each diatomic unit cell of the metasurface includes two nanoholes, with radii r_0 and r_1. Unit cells are spaced at a pitch, P. Crucially for our devices, we will show that P can be

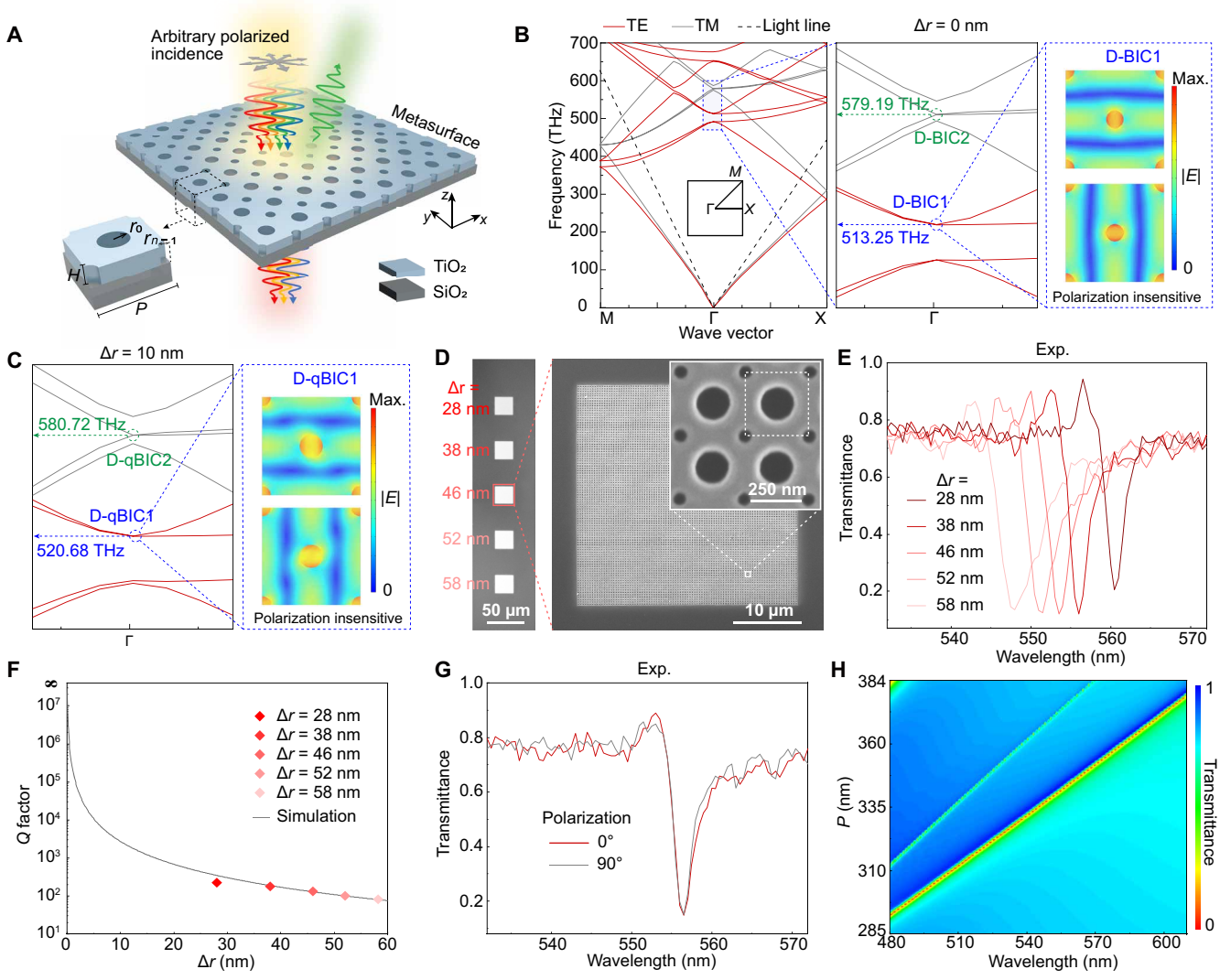

Fig. 2. Pixelated metasurfaces with polarization-independent qBICs. (**A**) Schematic diagram of the as-designed diatomic metasurface, formed from cylindrical nanoholes, arranged in a square lattice, and etched into a TiO_2 slab with thickness $H = 92$ nm. Unit cells (left) spaced at a pitch P, compose of diagonally arranged holes with two different radii, r_0 and r_1. (**B**) Band structures and field distributions of such a metasurface when $\Delta r = r_0 - r_1 = 0$ nm. The middle panel shows a magnified region of the band structure near the doubly degenerate BICs. The right panel shows the field distributions of D-BIC1. (**C**) Band structure near D-qBIC, and corresponding field distributions of D-qBIC1 when $\Delta r = 10$ nm. (**D**) SEM images of a fabricated 1 × 5 qBIC-based metasurface filter array with $\Delta r = 28$, 38, 46, 52, and 58 nm, respectively. (**E**) Measured transmitted spectra at varying values of Δr. (**F**) Q factor of D-qBIC1 extracted from simulated and measured (E) transmitted spectra. (**G**) Measured transmission spectra under 0 and 90° polarizations, demonstrating a polarization-independent response. (**H**) Simulated metasurface transmission spectra for 100 filters with varying unit cell pitch, P. For all other demonstrations in this figure, $P = 338$ nm.

varied to tune the central wavelength of the metasurface's bandstop transmission feature, while $\Delta r = r_0 - r_1$ can be tuned to vary the FWHM of the transmission feature. The nanoholes are etched into a titanium dioxide (TiO_2) film deposited onto quartz at a thickness $H = 92$ nm. Here, TiO_2 provides low absorption while retaining sufficient index contrast with the quartz substrate (See the "Device fabrication" section in Materials and Methods). When $r_0 = r_1 = 30$ nm, due to the band folding mechanism and the C4v symmetry of the metasurface (*21*, *22*), simulations show that the metasurface has doubly degenerate BICs (D-BICs) at Γ, which can be decomposed into two orthogonal dipole-like modes that are a 90° rotation of each other (see Fig. 2A). In our metasurface design, there are two pairs of D-BICs: a transverse-electric (TE)–like mode at 513.25 THz (D-BIC1) and a transverse-magnetic (TM)–like mode at 579.19 THz (D-BIC2), respectively. They have similar physical characteristics and origins, and so for simplicity, we focus here on the analysis of D-BIC1 (see the "Numerical analysis of BIC" section in Materials and Methods and also section S2). We introduce variations in r_0 so that Δr is nonzero; this geometrical perturbation breaks the original translation symmetry but preserves the C4v symmetry of the metasurface. In this way, the D-BICs degrade to doubly degenerate quasi-BICs (D-qBICs) that are slightly coupled to the radiation continuum (see Fig. 2C) and that have finite but large Q factors (see the "Numerical analysis of BIC" section in Materials and Methods).

To experimentally confirm the characteristics of these D-qBICs, we fabricated five metasurfaces with $\Delta r = 28$, 38, 46, 52, and 58 nm, respectively. A full simulation of the relationship between metasurface transmission and the geometrical perturbation, Δr, is shown in section S3. Figure 2D shows scanning electron microscopy (SEM) images of the metasurface slab array. Q factor values derived from both numerically simulated and experimentally measured (Fig. 2E) transmission spectra are displayed in Fig. 2F. There is an inverse quadratic dependence between the Q factor and Δr, and the Q factor tends to infinity when $\Delta r = 0$, as commonly seen in qBICs (*18*). The experimental results are in good agreement with the simulated counterparts. For $\Delta r \leq 40$ nm, the reduction in the actual Q factor relative to simulations can be attributed to linewidth broadening of the transmitted spectra due to measurement limitations imposed by the monochromator's resolution and SNR. Moreover, because of the preservation of C4v symmetry, the D-qBICs have been designed to be equally sensitive to light regardless of polarization (Fig. 2G) (*21*, *22*) and, hence, do not require a polarizer to filter the input light, further increasing the throughput of photons to the detector array. Crucially, we show through simulation the transmissive properties of D-qBICs as a function of P (while maintaining fixed Δr; Fig. 2H), confirming that D-qBICs can function as tunable and narrow bandstop filters through modification of the P value, enabling their use for spectral sensing in the visible range.

qBIC spectrometers

Next, we demonstrate a high-performance microspectrometer based on our qBIC metasurface filters. Instead of a direct read-out, our spectrometer uses an array of qBIC metasurfaces, mounted on to a CMOS image sensor (Fig. 3A), to sample a light signal before computationally reconstructing the spectra. Represented mathematically, the light intensity incident on each of the detectors I_i is a convolution of the incident spectrum $S(\lambda)$ and the transmitted profile $T_i(\lambda)$, given by a system of linear equations (*4*, *12*)

$$\int_{\lambda_1}^{\lambda_2} S(\lambda)T_i(\lambda)d\lambda = I_i \qquad (i = 1, 2, 3 \ldots, m) \tag{1}$$

where m is the detector number. By solving the system of equations for all detectors via a reconstruction algorithm (see the "Reconstruction algorithms" section in Materials and Methods), which also works to minimize the effects of measurement noise, we can arrive at an approximation of $S(\lambda)$.

The device is composed of a 10 × 10 metasurface filter array (Fig. 3B) with P values varying linearly between 285 and 384 nm across the 100 filters and the operational wavelengths of the corresponding metasurface filters across 480 to 610 nm. Note that the operational wavelengths can be extended to other spectral regions simply via adjustments in both P and Δr. The metasurface filter array is designed

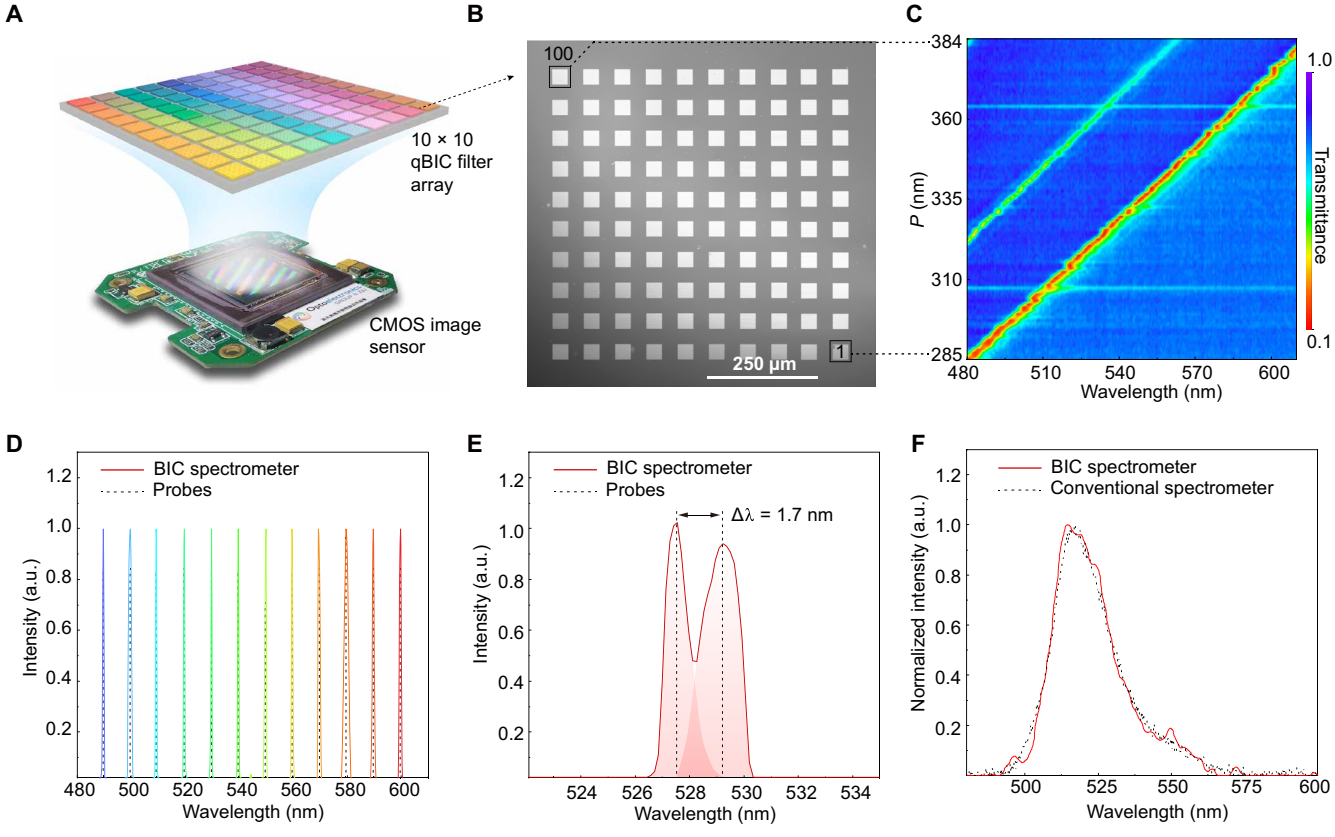

Fig. 3. Microspectrometer based on qBIC metasurfaces. (**A**) Schematic of the spectrometer featuring an individual 10 × 10 qBIC bandstop filter array integrated atop a CMOS imaging sensor. (**B**) SEM image of the fabricated metasurface filter array. (**C**) Bandstop transmission profiles $t_i(\lambda)$ of the 100 filters. (**D**) Measured, reconstructed spectra of a series of monochromatic spectral lines (dark dotted lines) in the visible range. (**E**) Measured, reconstructed spectrum of two narrow spectral lines, demonstrating ability to resolve distinct monochromatic spectral features down to 1.7-nm separation. (**F**) Measured, reconstructed spectrum of a broadband light source, relative to the same incident signal measured by a conventional spectrometer. a.u., arbitrary units.

with a fixed Δr at 46 nm. This is a compromise between lowering Δr to achieve higher resolutions while being constrained by the limits of the transmission function calibration system and the noise level of the CMOS sensor array, as discussed in the section S2.

As shown in Fig. 3C, the transmission profiles $t_i(\lambda)$ of the metasurface filter array are measured under a customized micro-area ultraviolet-visible spectrophotometer and show good agreement with the simulated responses in Fig. 2H. We note that the secondary bandstop feature seen at lower wavelengths does not interfere with the function of the spectrometer, as it is accounted for in the calibration of the system. Measurement of the spectral response profiles for the system as a whole, $T_i(\lambda)$—a combination of the filters' transmission profiles $t_i(\lambda)$ and the photoresponse profiles $R_i(\lambda)$ of the CMOS pixels—is discussed in the Supplementary Materials (see the "Calibration" section in Materials and Methods). While operating, under illumination by an arbitrary light signal with spectra $S(\lambda)$, the CMOS image sensor measures the set of light intensities, I_i, transmitted through the metasurface filter array. As described earlier in Eq. 1, the I_i measured at each detector represents a set of linear equations, integrals of the incident spectrum $S(\lambda)$ and $T_i(\lambda)$ over the wavelength range; $S(\lambda)$ can be reconstructed by solving the inverse problem posed by this dataset. In practice, such a calculation is ill-posed and highly susceptible to experimental noise; hence, an algorithm was developed to solve the set of linear equations generated by the encoders, the details of which are discussed in the "Reconstruction algorithms" section in Materials and Methods.

To demonstrate the accuracy of the device, we tested the reconstruction fidelity of the microspectrometer when resolving a series of narrow spectral lines across a range of 480 to 610 nm. The results by the spectrometer match the positions of the individual probe lines with a mean accuracy of ±0.11 nm and an average SNR of ~300 Fig. 3D. The dynamic range of spectrometer is ~500, calculated as the ratio of the detector saturation level and the lowest detectable intensity that we define as the power density incident on the detectors at the point where the signal is just indistinguishable from the noise floor. For evaluating the spectral resolution of the device, we use the Rayleigh criterion: That two spectral lines are just resolved when the maxima of the first peaks are positioned at the base of the second. As shown in Fig. 3E, this device enables a spectral resolution of 1.7 nm; such a resolution is comparable to that of most microspectrometer counterparts (*4*, *5*) [for reference, the resolution of a mature product, the Hamamatsu C12666MA microspectrometer, is 12 nm (*23*)]. Our metasurface spectrometer can also accurately reconstruct continuous broadband spectra across the operational wavelength span, as shown in Fig. 3F. The typical reconstruction time is only 0.2 s for each spectrum on a laptop, making it readily available for portable device.

Performance under ultralow irradiance

As discussed previously, the fundamental advantage of this qBIC-based system is that because of the nature of the spectral responses, the sensitivity should actually increase with resolution, rather than exhibiting a resolution-luminosity trade-off. As shown in Fig. 4A, to study the relationship between the resolution and sensitivity in our qBIC-based platform, five metasurface spectrometers were fabricated with different bandstop line widths, and their performance was studied with respect to resolution and the minimum detectable irradiance as a measure of their sensitivity. The spectrometers contain 16 metasurface filters with $\Delta r = 28$, 38, 46, 52, and 58 nm, corresponding to FWHMs of 2.8, 4.2, 5.6, 6.5, and 7.0 nm, respectively. For a controlled comparison, to make these five spectrometers work over the same spectral range, the lattice constants, P, of each array element covers 336 to 351 nm, 333 to 348 nm, 330 to 345 nm, 326 to 341 nm, and 321 to 336 nm, respectively, in steps of 1 nm. These results shown in Fig. 4A suggest first that (for a constant number of filters) a smaller linewidth does indeed lead to higher spectral resolution, confirming our simulated work in the section S1. We note that the maximum resolution of 1.9 nm achieved here is constrained by the number of filter array elements used (in this case, 16 filter elements); the ultimate resolution limit for this device could be much lower. More crucially, the minimum detectable irradiance increased in correlation with the measured resolution. This supports our assertion that these systems are not constrained by a resolution-luminosity trade-off and can be engineered to achieve high sensitivity and spectral resolution, simultaneously, unlike in equivalent narrowband filter array systems. Through direct comparison with an equivalent reconstructive device, we further confirm the advantages of our platform over narrowband systems in enhanced sensitivity through a greater utilization of available flux onto the detector (section S4).

The key strength of this platform is in providing high sensitivity so as to maximize the limited available light in highly miniaturized systems. We first demonstrate the real-world applicability of the qBICs metasurface spectrometer's sensitivity via fluorescence measurements of bacteria samples (see the "Spectroscopy measurements" section in Materials and Methods). The samples are characterized under three different illumination intensities, as shown in Fig. 4B. Comparisons between spectra measured by the qBICs metasurface spectrometer and a conventional mini-spectrometer are shown in Fig. 4C. As the excitation power decreases, the spectra measured by the conventional spectrometer become overridden by noise, while the qBICs metasurface spectrometer can still reconstruct the fluorescence spectrum. Enabling low-light excitation fluorescence measurements could help to avoid damage or photobleaching when measuring biological samples. Further to this, as shown in Fig. 4D, we use our platform to gather spectral data from the night sky through telescopic measurements of Venus (see the "Spectroscopy measurements" section in Materials and Methods). We show that even for clear conditions, where measurements become noise-dominated in a conventional device at an integration time of 1 s, our system produces clear data with an order of magnitude lower integration times (Fig. 4E). We note that the irradiance for both fluorescence and planetary demonstrations cannot be directly measured by a power meter; we estimate the stated values via the linear power response of the qBIC spectrometer (section S5). Furthermore, when cloudy conditions make measurement of the conventional system untenable, our device is still capable of collecting useful spectral data. We note here that through tuning the geometric parameters of the qBIC array, the operational range could be straightforwardly extended into the infrared (see section S6), which is of more relevance to many astrophotonic applications. Last, in Fig. 4F, we experimentally demonstrate the sensitivity advantages of a qBIC system by measuring light throughput onto the detector, in comparison with grating and filter strategies, at varying bandstop/bandpass FWHM; throughput in the qBIC system lies between one and two orders of magnitude higher than the conventional strategies.

DISCUSSION

We demonstrated that by engineering metasurfaces with qBICs, it is possible to produce the building blocks of a new paradigm of

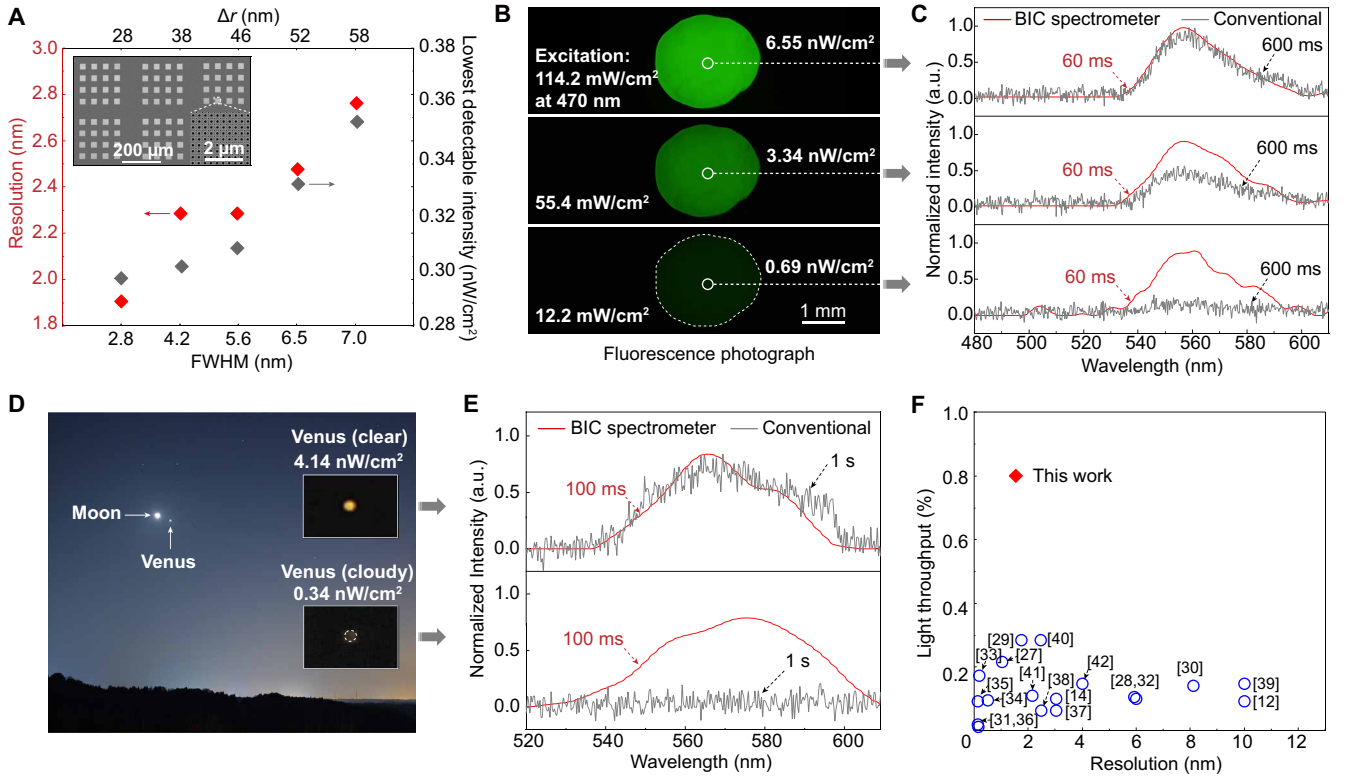

Fig. 4. Demonstration of the metasurface spectrometer for low-light level detection. (**A**) Resolution and lowest detectable intensity of five qBIC-based spectrometers with different values of Δ*r*, each composed of 16 metasurface filter units, demonstrating a positive correlation between resolution and sensitivity. Inset shows SEM images of the five different spectrometers and a magnification of one filter unit (bottom right). (**B**) Fluorescence photographs of bacteria under different excitation intensities and (**C**) corresponding spectra measured by a qBIC-based metasurface spectrometer (red) and conventional mini-spectrometer (black), respectively. (**D**) Colorful photograph of the night sky, with magnified insets showing Venus in clear and cloudy conditions. (**E**) Visible range spectra of Venus corresponding to clear (top) and cloudy (bottom) conditions from (D), as measured by our BIC spectrometer versus a conventional mini-spectrometer. For both (C) and (E), the conventional mini-spectrometer model is an Avaspec-uls2048cl (600/mm grating, 25-μm slit, 37,5000 counts/μW per ms integration time, which represents high-end commercial mini/microspectrometers). (**F**) Light throughput efficiency (expressed as eventual intensity onto the detectors as a percentage of total light intensity before spectral dispersion/selection) and resolution of a selection of state-of-the-art (reconstructive and conventional) miniaturized spectrometers (*12, 14, 27–42*).

microspectrometers that are not bound by the same limits on sensitivity that constrain conventional filter array systems. Augmented by a computational spectral reconstruction algorithm, these devices offer a route toward a platform that maintains high resolution and sensitivity in a highly miniaturizable planar form. These devices could prove ideal for a wide range of low-light-level applications such as Raman measurements, astronomical spectrographs, and nanoscale biomedical spectroscopy.

MATERIALS AND METHODS

Device fabrication

The fabrication of our metasurface consists of two main steps: Deposition of a TiO_2 layer and the production of nanoholes in the TiO_2 film. TiO_2 films were deposited onto a quartz substrate via electron-beam evaporation. Substrates were first cleaned through successive ultrasonication steps in acetone, methanol, and deionized water, respectively, for 20 min each before electron-beam evaporation at a base vacuum of 2×10^{-7} torr and a deposition rate of 0.8 Å/s. After TiO_2 film deposition, absorptive coefficient, *k*, and refractive index, *n*, are characterized through ellipsometry. As illustrated in fig. S7, the absorption coefficient vanishes within the wavelength range of 480 to 610 nm, while the refractive index is approximately 2.3. As summarized in fig. S8, electron-beam lithography (EBL) and ion beam etching (IBE) processes were used to fabricate nanoholes in the films, ensuring high accuracy and precision.

A three-stage mask process was used, with an EBL patterned resist to mediate etching onto a chromium (Cr):gold (Au) layer, which in turn was used to etch an amorphous silicon (a-Si) film that acted as the final mask for the TiO_2. A 200-nm a-Si layer was first deposited by plasma-enhanced chemical vapor deposition (SYSTEM 100) on the TiO_2 film. This was followed by a 5-nm Cr adhesion layer and a 75-nm Au film, deposited by electron-beam evaporation (COOKE). A 300-nm photoresist (ARP) film was then spin-coated onto the chip and baked at 85°C for 90 s.

The designed nanohole lattice was patterned into ARP by an electron-beam writer (MA6, with an acceleration voltage of 30 kV) before development in REX3038 solution and deionized water at 25°C for 60 and 30 s, respectively. The Cr:Au mask layer was then etched using the IBE before etching of the a-Si layer through an inductively coupled plasma (ICP) process. The ARP and Cr:Au mask layers were then removed by an oxygen plasma and wet chemical etch, respectively. Last, the nanoholes were patterned into the TiO_2 layer by IBE through the Si mask before removal of the mask by another ICP etch.

The choice to use three masks (ARP, Cr:Au, and a-Si) was made as the TiO_2-etching gas readily etches photoresist, and thus, a hard mask is needed to pattern the TiO_2. Amorphous silicon was chosen as the hard mask material to avoid any influence on the optical properties of the BIC layer from metallic residues. However, to obtain an a-Si mask with accurately defined nanohole dimensions, the mask used to pattern it must be very thin (<100 nm); a resist mask of this thickness would be removed too quickly during the a-Si etch, so an Au mask is used instead, which itself can be first patterned via the EBL resist.

Numerical analysis of BIC

The studied metasurface can support two sets of D-qBICs in the frequency range of interest. The D-qBIC1 (D-qBIC2) are transverse electric-like (transverse magnetic-like) polarized, whose electric fields in the middle plane are out of the plane (in the plane). In the main text, we mainly focus on the D-qBIC1, as discussed in Fig. 2. Here, we show the magnetic field distribution of D-qBIC2 and their Q factor dependence on Δr, as illustrated in fig. S9. Compared with D-qBIC1, D-qBIC2 has a much larger Q factor and a much narrow FWHM in the case of the same Δr. As a result, the behavior of D-qBIC1 is by far the dominant factor in the operation of the spectrometer (section S2).

Simulated electric field distributions of D-BIC1 and D-qBIC1 in the yoz plane are displayed in fig. S12. It is seen that the field of D-BIC1 is strongly confined near the metasurface along the normal direction without any escaping radiation, implying an infinite Q factor. However, for D-qBIC1, we can observe that there is radiation out of the metasurface body, although the field is still localized along the normal direction of the metasurface, which makes qBIC an ideal candidate for optical spectrometers breaking the resolution-luminosity limit.

Reconstruction algorithms

The photoelectric response of the spectrometers' sensors can be expressed in the form of the integral equation (Eq. 1). For any set of response functions $T_i(\lambda)$ that are continuous over a bounded domain of $\Omega := [\lambda_1, \lambda_2]$, the reconstruction problem is inherently ill-posed, where the presence of a small perturbation in the response signal I_i could produce an infinitely large change in the reconstructed spectrum (*24*). Physically, this ill-posedness reflects the unavoidable information loss during the encoding procedure (Eq. 1), making the spectrum $S(\lambda)$ impossible to be directly obtained from the measurements I_i. If the incident spectrum $S(\lambda)$ can be well approximated by a function $\widehat{S}(\lambda)$ that lies in the function space spanned by basis functions φ_i with $j = 1, 2, \ldots, n$, then we can discretize the problem by the expansion

$$S(\lambda) \approx \widehat{S}(\lambda) = \sum_{j=1}^{n} \gamma_j \varphi_j(\lambda) \tag{2}$$

where the coefficients vector $x = \left[\gamma_1, \gamma_2, \cdots, \gamma_m\right]^T$. In our case, we discretized the spectrum $S(\lambda)$ using a piecewise polynomial and approximated the integral by Gaussian quadrature (*25*). Compared with Gaussian basis functions used in our previous studies (*13*), piecewise polynomials are more expressive and eliminate the need to manually select basis function parameters (i.e., FWHM of Gaussian bases), while the use of Gaussian quadrature ensures the exactness of numerical integration as long as the integrand is a polynomial with a fixed degree (*25*).

Then, problem (Eq. 1) can be transformed into a finite-dimensional least square problem in the form of

$$x_{\mathrm{LS}} := \min_x \frac{1}{2} \| Ax - b \|_2^2 \tag{3}$$

where $b := \left[I_1, I_2, \ldots, I_m\right]^T \in \mathbf{R}_+^m$ is the vector of photoelectric responses and A is the coefficient matrix with each element a_{ij} determined by the inner product of response function T_i and basis function φ_i over the bounded domain Ω.

To regularize problem (Eq. 3), we imposed both l_1 and l_2 regularization alongside with the non-negative constraint on x

$$x_{\alpha,\beta}^{\dagger} := \min_{x \geq 0} \frac{1}{2} \| Ax - b \|_2^2 + \alpha \| x \|_1 + \frac{1}{2}\beta^2 \| x \|_2^2 \tag{4}$$

where $L \in \mathbf{R}^{(n-1)\times n}$ is a first-order discrete gradient matrix that constrains the smoothness of the reconstructed solution. By using the non-negative constraint of x, the minimization problem (Eq. 4) can be expanded into a constrained quadratic programming problem

$$x_{\alpha,\beta}^{\dagger} := \min_{x \geq 0} \frac{1}{2} x^{\mathcal{T}} \left(A^T A + \beta^2 L^T L\right) x + x^T \left(\alpha 1_n - A^T b\right) \tag{5}$$

where $\mathbf{1}_n = [1, 1, \ldots, 1]^T \in \mathbf{R}_+^n$.

The two regularization terms serve different purposes. The l_1 norm will promote sparsity which ensures high-resolution reconstruction for narrow spectra, while the l_2 norm regularization on the gradient will increase the smoothness of the reconstruction, thus more effective for broad spectra. The relative importance of sparsity and smoothness is measured by regularization parameters α and β, respectively, which are selected using K-fold cross-validation (*26*).

Calibration

To calibrate the spectral characteristics of the proposed spectrometer, a homemade calibration setup was constructed. Because of the narrow FWHM of BICs, it is necessary to find a monochromatic light source for calibration that has a narrower bandwidth and, covering the operational range of our device, can be tuned in the wavelength region of 440 to 620 nm. As illustrated in fig. S14A, the light source used was a Xenon lamp (Microsolar 300), providing a white light source; a monochromator (CME-Mo301) was then used to disperse the light spatially, and the monochromatic light of wavelength was selected by tuning the position of a grating. Here, a bandpass filter is also used to remove the harmonic wave stemming from the grating in the monochromator. The FWHM of the output light is 0.5 nm. The calibration light is divided by a 50:50 splitter, with the two beams directed to the spectrometer chip and a commercial spectrometer, respectively. The commercial spectrometer is used to monitor the central wavelength and power of the calibration light. The spectrometer chip is realized by aligning and attaching the metasurface onto the sensor surface of a CMOS pixel array. The CMOS chip is from Indigo Inc. (model: S400MRU), with a pixel size of 6.5 μm by 6.5 μm. The commercial spectrometer is an Avaspec-uls2048cl, which operates with a resolution of 0.5 nm. Using the calibration setup, the spectral responses of the meta-spectrometer are characterized, as shown in fig. S14B. Here, it can be seen that the bandstop peaks are linearly dependent on the P value (i.e., pitch) of the nanohole lattice.

Spectroscopy measurements

To verify the high-throughput ability of the spectrometer chip, a weak fluorescence spectrum of bacteria is measured. The test setup for this experiment is shown in fig. S17. The LED source emits broadband light, from which the fluorescence excitation is selected using a bandpass filter of 420 to 485 nm. A beam splitter (BS1) is used to reflect the light onto a fluorescent sample via a 4× microscope objective. The same objective collects the fluorescence and the reflected excitation light. A 515-nm longpass filter removes residual excitation light, leaving only the fluorescence signal. The fluorescence is divided equally by a 50:50 beam splitter (BS2). One beam is incident on the metasurface-spectrometer, while the other one enters the commercial spectrometer. Adjustments are made so that the apertures of the commercial spectrometer and meta-spectrometer are conjugated, and henec, the fluorescence measured by the two spectrometers comes from the same point on the fluorescent sample.

The Venus measurement setup is shown in fig. S18 (A and B). Venus was photographed with an astronomical telescope CGEM-II-1100HD from Celestron Co. Ltd. The telescope has a Schmidt-Cassegrain configuration with an aperture of 11 inch and a focal length of 2800 mm. A lens with a ×5 magnification is used to focus the light captured by the telescope onto the BIC spectrometer. A 50:50 beam splitter is placed in front of the BIC spectrometer to split half of the light into the conventional, grating-based spectrometer. The BIC spectrometer and the conventional spectrometer have an aperture with the same size. Between the imaging lens and the beam splitter, a 412 to 569 nm bandpass filter FGB18 from Thorlabs and a 550-nm longpass filter CB550 from Yongxing-Sensing Co. Ltd are mounted to filter the Venus light to those within the operating wavelength of the BIC spectrometer. In addition, a 600-nm lowpass filter is also used to reduce noise from background infrared light. The clear image of Venus was taken at about 2100, and the cloudy one was taken at about 2140.

Supplementary Materials

This PDF file includes:

Sections S1 to S9
Figs. S1 to S23

REFERENCES AND NOTES

1. M. Manley, Near-infrared spectroscopy and hyperspectral imaging: Non-destructive analysis of biological materials. *Chem. Soc. Rev.* **43**, 8200–8214 (2014).
2. K. B. Bec, J. Grabska, C. W. Huck, Principles and applications of miniaturized near-infrared (NIR) spectrometers. *Chemistry* **27**, 1514–1532 (2021).
3. C. P. Bacon, Y. Mattley, R. DeFrece, Miniature spectroscopic instrumentation: Applications to biology and chemistry. *Rev. Sci. Instrum.* **75**, 1–16 (2004).
4. Z. Yang, T. Albrow-Owen, W. Cai, T. Hasan, Miniaturization of optical spectrometers. *Science* **371**, eabe0722 (2021).
5. A. Li, C. Yao, J. Xia, H. Wang, Q. Cheng, R. Penty, Y. Fainman, S. Pan, Advances in cost-effective integrated spectrometers. *Light Sci. Appl.* **11**, 174 (2022).
6. J. Kulakowski, B. d'Humières, Chip-size spectrometers drive spectroscopy towards consumer and medical applications, in *Photonic Instrumentation Engineering VIII* (SPIE, 2021), vol. 11693, pp. 194–202.
7. G. M. Yee, N. I. Maluf, P. A. Hing, M. Albin, G. T. A. Kovacs, Miniature spectrometers for biochemical analysis. *Sensors Actuat. A Phys.* **58**, 61–66 (1997).
8. J. F. James, R. S. Sternberg, *Design of Optical Spectrometers* (Chapman and Hall, 1969).
9. S. B. Utter, J. R. Crespo López-Urrutia, P. Beiersdorfer, E. Träbert, Design and implementation of a high-resolution, high-efficiency optical spectrometer. *Rev. Sci. Instrum.* **73**, 3737–3741 (2002).
10. U. Rieser, M. R. Krbetschek, W. Stolz, CCD-camera based high sensitivity TL/OSL-spectrometer. *Radiat Meas.* **23**, 523–528 (1994).
11. C. W. Hsu, B. Zhen, A. D. Stone, J. D. Joannopoulos, M. Soljačić, Bound states in the continuum. *Nat. Rev. Mater.* **1**, 16048 (2016).
12. Z. Yang, T. Albrow-Owen, H. Cui, J. Alexander-Webber, F. Gu, X. Wang, T.-C. Wu, M. Zhuge, C. Williams, P. Wang, A. V. Zayats, W. Cai, L. Dai, S. Hofmann, M. Overend, L. Tong, Q. Yang, Z. Sun, T. Hasan, Single-nanowire spectrometers. *Science* **365**, 1017–1020 (2019).
13. H. H. Yoon, H. A. Fernandez, F. Nigmatulin, W. Cai, Z. Yang, H. Cui, F. Ahmed, X. Cui, M. G. Uddin, E. D. Minot, H. Lipsanen, K. Kim, P. Hakonen, T. Hasan, Z. Sun, Miniaturized spectrometers with a tunable van der Waals junction. *Science* **378**, 296–299 (2022).
14. J. Bao, M. G. Bawendi, A colloidal quantum dot spectrometer. *Nature* **523**, 67–70 (2015).
15. N. Blind, E. Le Coarer, P. Kern, S. Gousset, Spectrographs for astrophotonics. *Opt. Express* **25**, 27341–27369 (2017).
16. F. Yesilkoy, E. R. Arvelo, Y. Jahani, M. Liu, A. Tittl, V. Cevher, Y. Kivshar, H. Altug, Ultrasensitive hyperspectral imaging and biodetection enabled by dielectric metasurfaces. *Nat. Photonics* **13**, 390–396 (2019).
17. A. Tittl, A. Leitis, M. Liu, F. Yesilkoy, D.-Y. Choi, D. N. Neshev, Y. S. Kivshar, H. Altug, Imaging-based molecular barcoding with pixelated dielectric metasurfaces. *Science* **360**, 1105–1109 (2018).
18. K. Koshelev, S. Lepeshov, M. Liu, A. Bogdanov, Y. Kivshar, Asymmetric metasurfaces with high-Q resonances governed by bound states in the continuum. *Phys. Rev. Lett.* **121**, 193903 (2018).
19. A. Kodigala, T. Lepetit, Q. Gu, B. Bahari, Y. Fainman, B. Kanté, Lasing action from photonic bound states in continuum. *Nature* **541**, 196–199 (2017).
20. B. Wang, W. Liu, M. Zhao, J. Wang, Y. Zhang, A. Chen, F. Guan, X. Liu, L. Shi, J. Zi, Generating optical vortex beams by momentum-space polarization vortices centred at bound states in the continuum. *Nat. Photon.* **14**, 623–628 (2020).
21. A. C. Overvig, S. C. Malek, M. J. Carter, S. Shrestha, N. Yu, Selection rules for quasibound states in the continuum. *Phys. Rev. B* **102**, 035434 (2020).
22. P. Vaity, H. Gupta, A. Kala, S. Dutta Gupta, Y. S. Kivshar, V. R. Tuz, V. G. Achanta, Polarization-independent quasibound states in the continuum. *Adv. Photon. Res.* **3**, 2100144 (2021).
23. Hamamatsu mini-spectrometer micro series C12666MA; www.hamamatsu.com/eu/en/product/optical-sensors/spectrometers/mini-spectrometer/C12666MA.html.
24. P. C. Hansen, Rank-deficient and discrete ill-posed problems: Numerical aspects of linear inversion (SIAM, 1998).
25. L. N. Trefethen, Exactness of quadrature formulas. *SIAM Rev.* **64**, 132–150 (2022).
26. T. Hastie, R. Tibshirani, J. H. Friedman, J. H. Friedman, *The Elements of Statistical Learning: Data Mining, Inference, and Prediction* (Springer, 2009).
27. Z. Wang, S. Yi, A. Chen, M. Zhou, T. S. Luk, A. James, J. Nogan, W. Ross, G. Joe, A. Shahsafi, K. X. Wang, M. A. Kats, Z. Yu, Single-shot on-chip spectral sensors based on photonic crystal slabs. *Nat. Commun.* **10**, 1020 (2019).
28. J. Meng, J. J. Cadusch, K. B. Crozier, Detector-only spectrometer based on structurally colored silicon nanowires and a reconstruction algorithm. *Nano Lett.* **20**, 320–328 (2019).
29. X. Zhu, L. Bian, H. Fu, L. Wang, B. Zou, Q. Dai, J. Zhang, H. Zhong, Broadband perovskite quantum dot spectrometer beyond human visual resolution. *Light Sci. Appl.* **9**, 73 (2020).
30. E. Huang, Q. Ma, Z. Liu, Etalon array reconstructive spectrometry. *Sci. Rep.* **7**, 40693 (2017).
31. N. Alshamrani, A. Grieco, B. Hong, Y. Fainman, Miniaturized integrated spectrometer using a silicon ring-grating design. *Opt. Express* **29**, 15279–15287 (2021).
32. H. Li, L. Bian, K. Gu, H. Fu, G. Yang, H. Zhong, J. Zhang, A near-infrared miniature quantum dot spectrometer. *Adv. Opt. Mater.* **9**, 2100376 (2021).
33. C. Sun, Z. Chen, Y. Ye, Y. Weng, K. Lei, H. Ma, M. Wei, C. Zhong, H. Lin, L. Li, Integrated microring spectrometer with in-hardware compressed sensing to break the resolution-bandwidth limit for general continuous spectrum analysis. *Laser Photon. Rev.* **17**, 2300291 (2023).
34. C. Sun, Z. Chen, Y. Yin, Y. Ye, Y. Luo, H. Ma, J. Jian, Y. Shi, C. Zhong, D. Zhang, H. Lin, L. Li, Broadband and high-resolution integrated spectrometer based on a tunable FSR-free optical filter array. *ACS Photon.* **9**, 2973–2980 (2022).
35. Z. Zhang, Y. Liu, Z. Wang, Y. Zhang, X. Guo, S. Xiao, K. Xu, Q. Song, Folded digital meta-lenses for on-chip spectrometer. *Nano Lett.* **23**, 3459–3466 (2023).
36. Z. Zhang, Y. Wang, J. Wang, D. Yi, D. W. U. Chan, W. Yuan, H. K. Tsang, Integrated scanning spectrometer with a tunable micro-ring resonator and an arrayed waveguide grating. *Photon. Res.* **10**, A74–A81 (2022).
37. D. Tua, R. Liu, W. Yang, L. Zhou, H. Song, L. Ying, Q. Gan, Imaging-based intelligent spectrometer on a plasmonic rainbow chip. *Nat. Commun.* **14**, 1902 (2023).
38. C. Zuo, L. Zhang, X. Pan, H. Tian, K. Yan, Y. Cheng, Z. Jin, C. Yi, X. Zhang, W.-Q. Wu, Q. Bao, L. Han, L. Ding, Perovskite films with gradient bandgap for self-powered multiband photodetectors and spectrometers. *Nano Res.* **16**, 10256–10262 (2023).
39. L. Kong, Q. Zhao, H. Wang, J. Guo, H. Lu, H. Hao, S. Guo, X. Tu, L. Zhang, X. Jia, Single-detector spectrometer using a superconducting nanowire. *Nano Lett.* **21**, 9625–9632 (2021).
40. J. J. Cadusch, J. Meng, D. Wen, V. R. Shrestha, K. B. Crozier, Compact, lightweight, and filter-free: An all-si microspectrometer chip for visible light spectroscopy. *ACS Photon.* **9**, 474–481 (2022).

41. J. Zheng, Y. Xiao, M. Hu, Y. Zhao, H. Li, L. You, X. Feng, F. Liu, K. Cui, Y. Huang, W. Zhang, Photon counting reconstructive spectrometer combining metasurfaces and superconducting nanowire single-photon detectors. *Photon. Res.* **11**, 234–244 (2023).
42. A. Bainbridge, R. E. Allen, C. J. McIndo, A. R. Marshall, *Quantum sensing and nano electronics and photonics XVIII* (SPIE, 2022), vol. 12009, pp. 10–15.

Acknowledgments: We thank D. Liu, H. Wu, F. Jing, Y. Gu, Y. Chen, H. Zhang, X. Luo, R. Qiu, C. Wang, Z. Li, Z. Zhan, T. Xu, and Z. Guan for discussion. We thank W. Zhang and J. Cui from Ideaoptics Co. Ltd and Q. Li from Sichuan Society for Amateur Astronomy for the experimental assistance. We also thank the Micro and Nano Fabrication Centre at Zhejiang University for facility support. **Funding:** This work was supported by the National Key R&D Program of China grants 2023YFB3405600 (to Z.Y.Y.), 2022YFB3206000 (to Z.Y.Y.), 2022YFA1404900 (to Y.H.Y.), and 2022YFA1405200 (to Y.H.Y.), National Natural Science Foundation of China grants 62334001 (to Z.Y.Y.) and U20A20172 (to S.D.), the leading innovation and entrepreneurship team project in Zhejiang 2022R01001 (to Z.Y.Y.), the Natural Science Foundation of Sichuan Province grant 2022NSFSC1728 (to L.Z.), the Zhejiang Province Key R&D programs grant 2021C05004 (to S.D.), and the Leverhulme Trust Early Career Fellowship grant ECF-2022-711 (to T.A.-O.). **Author contributions:** Conceptualization: F.T., Z.Y., X.Y., and Y.Y. Methodology: T.A.-O., F.T., J.W., J.L., L.Y., Y.Y., and H.Ch. Validation: J.W., Y.Su., B.J., and J.H. Formal analysis: H.Cu., F.C., F.T., X.G., E.A.M., and H.J.J. Investigation: J.W., F.T., H.Cu., T.A.-O., L.Z., J.C., W.Z., Z.S., L.C., and S.D. Visualization: Y.S., S.L., and B.L. Supervision: Z.Y., T.H., X.Y. and Y.Y. Writing—original draft Preparation: Z.Y., F.T., H.Cu., F.C., Y.Y., and L.Z. Writing—review and editing: T.A.-O., T.H., H.Cu., Z.S., Z.Y., X.Y., and Y.Y. **Competing interests:** The authors declare that they have no competing interests. **Data and materials availability:** All data needed to evaluate the conclusions in the paper are present in the paper and/or the Supplementary Materials.

Submitted 15 July 2024
Accepted 4 November 2024
Published 6 December 2024
10.1126/sciadv.adr7155